



1 **Performance Evaluation for Retrieving Aerosol Optical Depth from**
2 **Directional Polarimetric Camera (DPC) based on GRASP Algorithm**

3
4 Shikuan Jin ¹, Yingying Ma ^{1,2,*}, Cheng Chen ⁴, Oleg Dubovik ⁵, Jin Hong ⁶, Boming Liu ¹, Wei
5 Gong ^{2,3}
6

7 ¹ State Key Laboratory of Information Engineering in Surveying, Mapping and Remote Sensing,
8 Wuhan University, China.

9 ² Collaborative Innovation Center for Geospatial Technology, Wuhan 430079, China.

10 ³ School of Electronic Information, Wuhan University, China.

11 ⁴ GRASP-SAS, Remote Sensing Developments, Cite Scientifique, University of Lille, 59655
12 Villeneuve d'Ascq, France.

13 ⁵ Univ. Lille, CNRS, UMR 8518 - LOA - Laboratoire d'Optique Atmosphérique, Lille, France.

14 ⁶ Anhui Institute of Optics and Fine Mechanics, Chinese Academy of Sciences, Hefei 230031,
15 China.

16
17 Corresponding Author: Yingying Ma (yym863@whu.edu.cn)

18 **Abstract**

19 Aerosol spatial distribution obtained from the satellite sensor is a critical point to understand
20 regional aerosol environment, anthropogenic aerosol emissions, and global climate change. In this
21 study, the performance of aerosol optical depth (AOD) retrieval from the Directional Polarimetric
22 Camera (DPC)/GaoFen-5 by using the Generalized Retrieval of Atmosphere and Surface Properties
23 (GRASP) algorithm was evaluated on a global basis for the first time. The results showed that the
24 DPC GRASP/Model scheme, which used several aerosol-type mixings, achieved good performance.
25 By compared with AERONET observations, the correlation coefficient (R), normalized mean square
26 error, and Expect Error (EE%) were 0.8982, 0.1008, and 83.16%, respectively. The scattering angle,
27 number of averaged pixels in retrieval units, and radiative and polarized fitting residuals showed
28 impacts on the results of AOD retrieval in the DPC GRASP/Model. From the most of AERONET
29 sites, the R and EE% were larger than ~0.9 and ~80%. Compared with MODIS products, the spatial
30 and temporal variations of AOD could be caught by the DPC observations with the GRASP/Model,
31 and compared with the MODIS Dark Target algorithm, the DPC GRASP/Model AOD also showed
32 a good performance. The above findings validated the ability of DPC sensor to monitor aerosols. It
33 would contribute to the development of aerosol parameter retrieval from multi-angular polarized
34 sensors in the future.

35
36 **Key Words:** GRASP/Model, Aerosol Optical Depth, Directional Polarimetric Camera, GaoFen-5,
37 Aerosol Parameter Retrieval
38



39 1. Introduction

40 Aerosol is one of the most important components in the atmosphere. They influence the global
41 radiation budget balance and climate directly by scattering and absorbing incoming solar radiation
42 and indirectly by changing cloud microphysical properties (Albrecht 1989; D'Almeida et al. 1991;
43 Rosenfeld et al. 2008). Due to the different emission sources and relatively transitory lifecycle in
44 the atmosphere, aerosol particles show large spatiotemporal variability, and it is difficult to describe
45 uniformly at a global scale (Eck et al. 2010; Jin et al. 2019; Ma et al. 2021). This property can further
46 affect the atmospheric motion, hydrological cycle, and probably contribute regional extreme
47 weather events (Nakajima et al. 2007; Guo et al. 2016; Li et al. 2016; Shi et al. 2021). Therefore,
48 the development of aerosol measurement technologies has been a topic received widely attention in
49 recent decades.

50 Satellite observation is the mainly approach to monitor and quantify aerosol distributions at a
51 global scale (Kaufman et al. 1997). Traditional Satellite technology relies on unique channel design
52 and prior assumptions about the properties of the surface and atmosphere, because the prerequisite
53 for successful retrieval of aerosol is that the aerosol signal should be isolated from a total mixture
54 of information received by satellite, which includes the combined effect from molecule, aerosol,
55 cloud, and the underlying surface (Lenoble et al. 2013). For instance, the appropriate spatial
56 resolution helps to observe aerosol through clear holes in otherwise cloudy skies (Jin et al. 2021).
57 The choice of spectral channel and bandwidth can avoid impact by gas absorption, if they are in
58 narrow spectral bands of atmosphere window regions. In addition, more importantly, the spectral
59 channel should be set in a carefully selected band to avoid introducing uncertainty from underlying
60 surface features in the meantime, such as vegetation, bright desert, and ocean color (McCormick et
61 al. 1979; Rao et al. 1989; Hsu et al. 2004). Based on these principles, a series of aerosol products
62 from different sensors has been released, and they greatly promote the developments of studies in
63 aerosol-related fields, including aerosol climate effect, interaction of aerosol and cloud, air quality
64 and public health, and global climate modeling (Tegen and Lacis 1996; Sayer et al. 2013; Gao et al.
65 2017; Zhang et al. 2021).

66 With the progress of satellite technology, sensors with broader spectral range, multiple angles,
67 and polarization observations have also been applied to aerosol observations. The POLDER-3 is the
68 third sensor in the POLarization and Directionality of the Earth's Reflectance series, carried on the
69 Polarization and Anisotropy of Reflectances for Atmospheric Science coupled with Observations
70 from a Lidar (PARASOL), which was launched on December 18, 2004, as part of the A-Train (Tanre
71 et al. 2011). This instrument views ($\pm 51^\circ$ along track and $\pm 43^\circ$ across track) Earth from ~ 13 different
72 angles by using a set of wide-field telecentric optics and a rotating filter wheel in nine spectral
73 channels from 443 to 1020 nm (Deschamps et al. 1994). Among them, three channels in 490, 670,
74 and 865 nm have polarization observation capabilities. The POLDER-3 provides the longest multi-
75 angle polarimetric observation record of the Earth-atmosphere system in space to date and the
76 PARASOL mission was terminated in December 2013 due to limited on-board fuel budget. The
77 Directional Polarimetric Camera (DPC) is the first Chinese multi-angle polarized earth observation
78 satellite sensor, onboard the fifth satellite (GaoFen-5) of the Chinese High-resolution Earth
79 Observation Program (Li et al. 2018). It was launched successfully on May 9, 2018, with the
80 purposes of measuring aerosol parameters and providing information for the assessment of urban
81 air pollution. The design of DPC is similar to the POLDER-3. It is equipped five non-polarized



82 bands at 443, 565, 763, 765, and 910 nm and three polarized bands at 490, 670, and 865 nm, with
83 relatively higher spatial resolution of 3.3 km, that can observe Earth from ~9 different angles.
84 Therefore, the DPC occupies an important position in the development of polarization instruments
85 in China, and is expected to provide beneficial information for atmospheric aerosol monitoring and
86 satellite payload research.

87 The multi-angular polarized sensor can provide much more observations for the same pixel in
88 aerosol parameter retrieval. Compared to traditional spectral measurement, the multi-angle can help
89 constrain bidirectional reflections function, reducing uncertainty from the surface (Diner et al. 1998),
90 while the polarized signal is mainly from atmospheric aerosol and sensitive to particle microphysical
91 properties (Mishchenko and Travis 1997). Generally, the polarized signal can be considered as an
92 independent source of information. A well-known advantage is that the polarized light from the
93 surface is accounts for a small part of the total polarized light compared with that from the particles
94 and shows a feature of almost wavelength independence. In the algorithms for POLDER, the
95 polarized signals at 670 and 865 nm are used for deriving the best aerosol model over the ocean and
96 retrieving Aerosol Optical Depth (AOD) over land, due to the sensitivity to fine particles (Nadal
97 and Bréon 1999; Deuzé et al. 2001; Kacelenbogen et al. 2006; Ge et al. 2020). In addition, the
98 existence of the cloudbow effect in polarized signal can also be used to recognize cloud mask and
99 detect cloud structure (Breon and Goloub 1998; Breon and Colzy 1999; Li et al. 2021).

100 However, the algorithms that retrieve aerosol parameters from only one or two polarized
101 channels are still difficult to obtain complex aerosol optical and microphysical parameters, such as
102 aerosol size distribution and absorbing and scattering properties. To solve this problem, the
103 Generalized Retrieval of Atmosphere and Surface Properties (GRASP) algorithm is developed,
104 which provides a novel statistical optimized strategy that allows all aerosol-related measurement
105 data from multi-angular polarized sensors to participate in the retrieval (Dubovik et al. 2014). It
106 points out that the measured redundancy provided by multi-angular polarized sensor is considered
107 to be positive and useful, especially when the observations are larger than the unknowns (Dubovik
108 et al. 2011). At present, the GRASP algorithm has been successfully applied to a variety of sensors
109 to retrieve complex aerosol parameters, including POLDER, lidar, and sun photometer (Li et al.
110 2019; Chen et al. 2020; Lopatin et al. 2021). In this study, we retrieved AOD from DPC observations
111 by using GRASP algorithm and evaluated possible error influencing factors. At the same time, by
112 comparing MODIS and AERONET observations, the aerosol monitoring performance of DPC were
113 verified in different space and time scales. This will partially lay the foundation for the retrieval of
114 aerosol parameters from multi-angular polarized sensors in the future of China.

115 2. Satellite and Ground-based Data

116 2.1 DPC Data

117 The DPC is a multi-angular polarized sensor carried on the GF-5 satellite, which was launched
118 in May 9, 2018. This sensor completes a scan of entire Earth's surface about every two days at a
119 sun-synchronous orbit and provides a swath of 1850 km with a spatial resolution of 3.3 km (Li et
120 al. 2018). The DPC contains eight bands from 443 to 910 nm with a bandwidth of 10-40 nm that
121 can observe earth from ~9 different angles in a local time of ~13:30 PM. Except for water vapor
122 band (910 nm) and pressure bands (Oxygen A band: 763 and 765 nm), other five bands (443, 490,



123 565, 670, and 865 nm) are designed for observing aerosol (Li et al. 2018). The polarimetric
124 capability at 490, 670, and 865 nm is realized by a polarized filter wheel (0° , 60° , and 120°) and a
125 step motor (Hagolle et al. 1999). The laboratory calibration uncertainties are relatively 5% for
126 normalized radiation and absolutely 0.02 for Degree Of Linear Polarization (DOLP) (Li et al. 2021).
127 An in-flight calibration study showed that the radiometric calibration error increased to $\sim 9\%$ at 865
128 nm and the polarimetric calibration error increase to ~ 0.04 at 490 and 670 nm after launch, by
129 respectively applying Rayleigh and glint scenes over ocean (Qie et al. 2021). While, degradation of
130 instrument performance over time may result in higher negative radiometric shift (Zhu et al. 2022).
131 Thus, additional correction coefficients were also applied in this study to correct the image of the
132 DPC observations from March to April, 2020. For preparing to retrieve AOD, the processing of
133 DPC data is described in Section 3.2 in detail.

134 2.2 MODIS aerosol products

135 The Moderate-resolution Imaging Spectroradiometer (MODIS) has been in service for over
136 two decades, providing valuable data for the earth's observations. The MODIS Level 2 C6.1 aerosol
137 product (MxD04) is generated by using Dark Target (DT) algorithm and Deep Blue (DB) algorithm
138 (Hsu et al. 2013; Levy et al. 2013). It provides multi-wavelength AOD data from each individual
139 image with spatial resolutions of 3 km and 10 km. While, the MODIS Level 2 C6 aerosol product
140 (MCD19A2) considers temporal and spatial correlation of aerosols, calculating aerosol parameters
141 by using the Multi-Angle Implementation of Atmospheric Correction (MAIAC) algorithm from the
142 continuous scenes of two satellites (Terra and Aqua), with a spatial resolution of 1 km (Lyapustin
143 et al. 2018). Compared to global coverage of DT algorithm, the DB algorithm is only applied over
144 land, and the MAIAC algorithm is used over land and part of the surrounding ocean. These MODIS
145 aerosol products have been rigorously tested and verified, and are widely used in aerosol-related
146 studies (Sayer et al. 2014; Che et al. 2019; Zhdanova et al. 2020). Only MODIS data with the highest
147 quality were used in this study.

148 2.3 AERONET observations

149 The AERosol RObotic NETwork (AEROENT) is a federation of ground-based remote sensing
150 aerosol networks, established and expanded by various institutions from different countries (Holben
151 et al. 1998). It has contributed continuous and long-term aerosol optical, microphysical, and
152 radiative properties for more than 25 years in major ecosystems and human activity areas around
153 the world. The AOD data used for validation were acquired from Level 1.5 and Level 2.0
154 AERONET products, which have been cloud-screened and quality controlled. The uncertainties of
155 AOD are less than 0.02 (Eck et al. 1999). In order to match the AERONET data to the satellite
156 observations, a common approach is followed to averages satellite data within ± 30 min and a circle
157 of 0.25° (~ 25 km) radius centered at the selected site (Sayer et al. 2013). The relationship between
158 multi-wavelength AOD proposed by Ångström (1964) was applied to calculate the AOD at
159 corresponding wavelength of satellite bands from AERONET data.

160 3. Methods

161 3.1 Introduction of GRASP algorithm



162 GRASP is an open-source software package (<https://www.grasp-open.com/>) for calculating
163 and retrieving various optical and microphysical properties of aerosol and surface from observations
164 of different remote sensing instruments, such as satellite, lidar, radiometer, and radiosonde (Dubovik
165 et al. 2021). It was originally designed to improve and solve the problem of aerosol retrieval under
166 high surface reflectance conditions from the PARASOL observations (Dubovik et al. 2014), while
167 now has become a scientifically rigorous and versatile algorithm based on generalization principles
168 that works with diverse remote sensing applications in the community after continuous development
169 (Dubovik et al. 2021). The GRASP algorithm contains two pivotal and independent modules. One
170 is used to calculate the scattering, absorbing, and extinction of light between different media from
171 the physical level, simulating theoretical observational radiation signal, called “Forward Model”. It
172 allows define various complex aerosol (size distribution, refractive index, and sphere fraction, etc.)
173 and surface properties (Bidirectional Reflectance/ Polarization Distribution Function, BR/PDF, etc.)
174 in the construction of model. Therefore, this makes it possible to transform from optical observations
175 to aerosol microphysical properties and estimate the surface parameters in the meantime (Dubovik
176 et al. 2011). The other module can be thought of as general mathematical operations without any
177 particularly physical nature, called “Numerical Inversion”. It follows the statistically optimized
178 strategy to fit observations under the fundamental frameworks of the Maximum Likelihood Method
179 and multi-term Least Square Method (Dubovik and King 2000). By introducing Lagrange multiplier
180 method, the GRASP also realizes multiple-pixel retrieval, which constrains the variability of aerosol
181 and surface optical properties in fitting process by an extra prior knowledge. Due to the consideration
182 of the surrounding pixel information, the multi-pixel retrieval is more stable, and more importantly,
183 it can make up for the lack of aerosol reflection information in some cases, such as conditions that
184 the signal from aerosol is much less than that from the surface (Dubovik et al. 2011). Based on the
185 above advantages, the GRASP supports input measurements/parameters from different sources and
186 levels, such as normalized and polarized radiance, vertical extinction and backscatter profile, and
187 optical depth. This avoids that the traditional look-up table-based methods are difficult to apply to
188 each other, due to the limitations of different sensor channel and characteristic.

189 3.2 Pre-processing of DPC Data

190 In order to partially offset the signal attenuation due to possible instrument aging, before the
191 pre-processing and retrieval, the radiance signals from the DPC were transferred and corrected to
192 normalized radiative and polarized reflectance at top of the atmosphere.

$$193 [I_N, Q_N, U_N]^T = \pi \cdot [I, Q, U]^T / [E_0 \cdot A'_k(\theta_0) \cdot P'_k(\theta)] \quad (1)$$

194 where, the $[I, Q, U]^T$ are represent the radiative and polarized radiances, received by the DPC, in
195 the form of the first three parts of the Stokes vector. The $A'_k(\theta_0)$ and $P'_k(\theta)$ are the two additional
196 correction coefficients. For I , they are applied following the results of Zhu et al. (2022), which are
197 depended on the view zenith angle (θ) and calculated based on Rayleigh scenes over sea surface.
198 For polarimetric signals, the additional correction coefficients can be referred to Qie et al. (2021).
199 The E_0 is the standard solar radiation flux and the $[I_N, Q_N, U_N]^T$ are the corrected normalized
200 signals at top of the atmosphere of DPC.

201 In successful AOD retrieval, one of the key processes is to screen appropriate pixels. Cloud
202 pixel is the main factor impacting aerosol retrieval, because they will block the signal from aerosol
203 due to high reflectance, large coverage, and relatively high vertical position. Even very thin cirrus
204 clouds and missed cloud edges can cause an obviously positive error of ~13% in visible channel



205 (Koren et al. 2007). To remove cloud pixels in DPC images, we used several universal methods by
206 considering cloud-sensitive characteristics in radiative and polarized bands:

207 1) The first step is to filter the image with a 3×3 sliding window in blue (490 nm) and red (670
208 nm) bands for land and sea surfaces, respectively (Remer et al. 2012). If the standard deviation of a
209 window is greater than 0.0025, then the center pixel will be marked as a cloud pixel and removed
210 (Martins et al. 2002). This method was initially applied to the MODIS image by considering the
211 spatial variability of aerosol and cloud pixels. In addition, a threshold of > 0.4 in the green (565 nm)
212 band is also used to detect cloud pixels after the filter process, in accordance with the DT algorithm.
213 This threshold is to exclude very uniformly distributed cloud pixels in the central area of thick clouds,
214 and some snow pixels and glint area will also be excluded at the same time.

215 2) In second step, a whiteness test was applied by using reflectance in visible bands. It uses the
216 characteristic that clouds are white in the visible band, considering that pixel with the absolute value
217 of average relative deviations greater than 0.7 is cloud. In the absence of infrared and thermal
218 infrared information, it can supplementally remove any pixels that have flat reflectance, similar to
219 some operators using reflectance ratio to detect clouds. This method was proposed by Gomez-Chova
220 et al. (2007) for Medium Resolution Imaging Spectrometer (MERIS) multispectral image, and it
221 has also been considered in the well-known Fmask algorithm.

222 3) The third step used polarized bands to remove cloud pixels, following a fact that cloud drops
223 can show a relatively strong polarized reflectance by multiple scattering (cloudbow effect) under a
224 specify observation geometry. This feature has been used to generate cloud mask product for both
225 POLDER and DPC sensors (Breon and Colzy 1999; Li et al. 2021). When the scattering angle (SCA)
226 is between 127° and 157° , pixels with corrected polarized radiation at 865 nm larger than 0.03 and
227 0.05 for ocean and surface, respectively, are defined as cloud (Li et al. 2021). The relatively large
228 SCA range is for a strict screening, given that the main peak of the polarized reflectance by cloud
229 water droplets is $\sim 142^\circ$ (Goloub and Deuze 1994). In addition, any obvious noise is also removed
230 in this step, such as the case of $DOLP > 1$.

231 3.3 Construction of Multi-pixel Retrieval Unit

232 Next, we will explain the necessary operations and settings of parameters to apply the GRASP
233 algorithm to DPC data in detail. The GRASP algorithm can use the temporal and spatial continuity
234 of pixels, and allow a group of pixels to be inverted at the same time. The multi-pixel retrieval unit
235 for DPC in the study is shown as **Figure 1**. Each small cube represents a pixel in geographic grids
236 with a spatial resolution of $0.1^\circ \times 0.1^\circ$ (3×3 DPC pixel averaged). This is in accordance with the
237 MODIS 04_L2 product (~ 10 km). The projection is determined by the DPC data. Each pixel is
238 guaranteed to have at least 3 different observation angles. Size of the retrieval unit can be arbitrarily
239 selected, but limited by the hardware memory. Different colors show the percentage of land or sea,
240 and usually do not change with time. They need to be clearly defined in GRASP to select different
241 surface reflectance models. Cloud and no-data pixels need to be removed before the retrieval,
242 because the cloud flag setting has not been implemented in the current version of code. Finally, this
243 retrieval unit was applied in the GRASP to calculate the AOD distributions and compared with
244 AERONET observations.

245 3.4 Settings of Retrieval Parameters

246 The settings of initial value and spatial-temporal constraint can significantly impact results of



247 the statistically optimized strategy in the GRASP algorithm (Dubovik et al. 2011). The GRASP
248 allows different strategies to fit observations. As the cases recorded in the GRASP software, there
249 are two retrieval schemes. The configurations of the two schemes are different only by settings of
250 aerosol size distribution in the forward model. One fits the aerosol size distribution with 16 triangle
251 bins from the range of 0.05 to 15.0 μm , while the other uses 5 lognormal bins at 0.1, 0.1732, 0.3,
252 1.0, and 2.9 μm , based on pre-calculated optimized kernels of the POLDER-3. The 5 lognormal bins
253 scheme increases speed by ~ 9 times (2.5GHz CPU) without any graphical acceleration compared
254 to the 16 triangle bins scheme, and it has been used to generate the operational PARASOL/GRASP
255 aerosol products (Chen et al. 2020). In addition, there is a scheme that is being tested called
256 “GRASP/Model”. This fits observational signal by externally mixing several aerosol types with
257 fixed optical parameters, which is more stable and faster to calculate the AOD.

258 A tolerable absolute error in radiative transfer calculations is set to 0.0005 and the multiple
259 scattering effects has been considered. Number of atmospheric layers is set to 10 with an exponential
260 distribution. The input data of the GRASP algorithm was both normalized radiative measurements
261 at 443, 490, 565, and 670 nm and DOLP of 490 and 670 nm. The initial guess of aerosol and surface
262 properties are default in the GRASP software. They comply with general principles and are applied
263 to calculate AOD at a global scale. The Ross-Li’s model (Li et al. 2001) and the Cox-Munk model
264 (Cox and Munk 1954) were used for modeling radiative (non-polarized) reflectance over land and
265 ocean, respectively, while, the surface polarized reflectance was following the method of Nadal and
266 Bréon (1999). Among them, the complex refractive index and surface properties are generally
267 allowed to be fitted as wavelength-dependent parameters in iterations. All constraints on values are
268 given a default sizeable range, such as the first parameter in the Ross-Li’s model allowed to vary
269 from 0.001 to 1.100. By light scattering calculations (Dubovik et al. 2006), all aerosol microphysical
270 parameters are converted into optical parameters to participate in radiative simulation. Spatial and
271 temporal constraints of variabilities of aerosol and surface properties are realized by using Lagrange
272 multiplier method. More details can be referred to Dubovik et al. (2021). In this study, the
273 GRASP/Model scheme was used to retrieve AOD from DPC. All calculations of the GRASP relied
274 on the supercomputing system in the Supercomputing Center of Wuhan University.

275 4. Results and Discussions

276 4.1 Validation of DPC/GRASP with AERONET

277 As shown in **Figure 2**, the AERONET observations were used as the references to estimate the
278 performance of AOD retrieval from DPC images based on the GRASP algorithm. Linear regression,
279 correlation coefficient (R), Normalized Mean Square Error (NMSE), Mean Bias (MB), percentage
280 falling into Expect Error (EE%), and matching Number (N) were also calculated. Overall, the DPC
281 GRASP/Model AOD matches the AERONET observations with an R of 0.8590, a MB of 0.0189,
282 and a NMSE of 0.1432. Nearly 80% of the GRASP/Model AOD retrievals fall within the expect
283 error bounds, showing a good performance without any quality control. While, the slope of linear
284 regression was 0.8438, less than 1. This means that under heavy aerosol loading, the DPC/GRASP
285 may underestimate the AOD. Although the additional radiometric correction factors were applied,
286 negative drift due to DPC instrument attenuation probably reduces signals from strong reflectance
287 and thus results lower values of AOD.



288 In order to further study the retrieval performance of GRASP/Model, control the quality of the
289 retrieval result from DPC data, we calculated the dependences of NMSE with retrieval residuals,
290 serial length and effective pixel number in retrieval units, and observation geometry, as shown in
291 **Figure 3**. The retrieval absolute MB showed an obvious increase when the SCA is large than 150° .
292 Critical observation conditions, such as pixels at the edge of the image, will probably result to a
293 larger error in both satellite sensor and forward model. By contrast, different viewing angle number
294 (3-11) have relatively little impact on the retrieval results, that the average absolute MB bias varies
295 between 0.0395 and 0.0541. The same phenomenon was also found in the **Figure 3c**. With increase
296 in length of retrieval units, the absolute MB was relatively stable, only fluctuating around 0.047.
297 This indicated that the fitting scheme for using the external mixing of different aerosol types in this
298 scheme of the GRASP/Model did not show much dependence of the length of the time series. By
299 contrast, the absolute MB showed a decrease trend with the number of averaged pixels, from 0.082
300 to 0.041. It means that the GRASP/Model is relative sensitive to surrounding pixels in the study. In
301 addition, the spatial-temporal constraints in the retrieval are also affected by Lagrange multipliers,
302 which can be customized in the configuration file.

303 Fitting residual is an important factor to estimate the quality of retrieval in GRASP. It was
304 found that the absolute MB showed a slight increase (from 0.047 to 0.063) when the radiative fitting
305 residuals were larger than 8%. While, the absolute MB had a trend to decrease first and then increase,
306 with increase in the polarized fitting residuals. Given that the DPC designed uncertainty is about 5%
307 for radiometric measurements and 0.02 for DOLP, the relatively large absolute MB (0.069) at 0.01
308 of the polarized fitting residuals is caused by overfitting of GRASP/Model. To summarize, the SCA,
309 number of averaged pixels, and fitting residuals showed the impacts on DPC GRASP/Model AOD
310 retrieval in this test. Pixels with $SCA > 150$, number of averaged pixels < 4 , non-polarized fitting
311 residual $< 8\%$, and $0.01 < \text{polarized fitting residual} < 0.08$, were removed as the low-quality
312 retrievals.

313 **Figure 4a** showed the scatterplots and density distributions of DPC/GRASP AOD versus the
314 AERONET observations after quality control. About a quarter of the points was removed. It was
315 found that the performance of AOD retrieval from DPC images showed an enhancement. For DPC
316 GRASP/Model, the R increased from 0.8590 to 0.8982, the EE% increased from 79.58% to 83.16%,
317 the NMSE decreased from 0.1432 to 0.1008, and the MB decreased from 0.0189 to 0.0176. The
318 slope of linear regression also showed a slight improvement with the value increasing from 0.8438
319 to 0.8867. **Figure 4b** displayed the relative frequency of differences between DPC and AEROENT
320 AOD. The peak values of deviation for DPC GRASP/Model were found at 0.0144, -0.0185, and -
321 0.0935 when the $AOD < 0.2$, $0.2 \leq AOD < 0.5$, and $AOD \geq 0.5$, respectively. This shows that the
322 MB drifts from positive to negative as AOD increases.

323 4.2 Evaluation of DPC AOD Performance at a Spatial Scale

324 The DPC AOD retrieved by the GRASP/Model was compared with AERONET observations
325 at each individual site to show a world-wide retrieval result as **Figure 5**. The R, NMSE, MB, and
326 EE% were calculated and displayed on sites where the matching number of pixels was larger than
327 10. In addition to the observation performance of the DPC itself, spatial variations in performances
328 of AOD retrieval greatly depend on settings of initial parameter and constraint in the GRASP,
329 whether they are in line with the local aerosol and surface environments. Results showed that the
330 GRASP/Model achieved a great performance in different regions. The high values of R (> 0.8) were



331 found in most regions, while the several lower values (~ 0.6) were mainly observed in North America
332 and South Africa. The NMSE showed the values of NMSE in most sites were less than 0.1. This
333 means that $\sim 70\%$ values of AOD retrieval matched the true values very well. In several sites, such
334 as western United States, the NMSE were larger than 2, revealing that the AOD has a relatively
335 larger deviation calculated from DPC images based on current parameter setting with the GRASP
336 algorithm in the regions. The values of AOD were overestimated (~ 0.05) in the most areas, as shown
337 in MB of **Figure 5c**. By contrast, the underestimations were found in high aerosol loading regions,
338 such as South Asia and North Africa, that MB values were between -0.02 and -0.06 , in accordance
339 with the slope of linear regression of less than 1. The EE% showed that over 80% of AOD retrieved
340 in sites can fall within the expect error. However, an abnormal relatively high EE% ($> 60\%$) from
341 GRASP/Model was also found in the western United States where the NMSE was large and R was
342 low. By compared with sites in central Africa, this phenomenon was probably due to the clean air
343 and extremely low aerosol content there, and thus the NMSE showed relatively larger. It is worth
344 noting that the parameterization in the GRASP/Model scheme is a globally consistent configuration
345 in this study and does not consider the characteristics between different regions. This means that it
346 is possible to achieve better results in local regions by adjusting different parameterizations.

347 To further estimate the performance of DPC/GRASP AOD, two regions were selected as cases
348 as shown in **Figure 6**. The MODIS MAIAC, DT, and DB aerosol products were used as comparisons.
349 It was noted that the DB algorithm was only executed over land in the C6.1 MODIS DB aerosol
350 products. It was found that the spatial coverage of GRASP/Model AOD from DPC over land was
351 slightly lower than the MAIAC MODIS aerosol products. In addition to the narrower field of view
352 and longer re-visit cycle on DPC (MODIS operated in two satellite: Terra and Aqua), the cloud mask
353 method probably also mis-classified the cloud-free pixels in heavy aerosol loading conditions. This
354 also partially resulted the underestimation of DPC AOD because the heavy aerosol loading pixels
355 are removed. Nevertheless, DPC still properly captures the spatial distribution of AOD. The highest
356 AOD values (> 1.0) in the southern part of China (mainly Guangdong and Guangxi) were caught
357 by the current retrieval strategy. This is in accordance with the three MODIS products. By contrast,
358 the AOD found in North China Plain and Centre China by the DPC GRASP/Model (~ 0.5) were a
359 little bit lower than MAIAC and DT products (~ 0.6). However, the DT aerosol products showed
360 higher AOD in this region, closed to ~ 1.0 . This phenomenon owes to unsuitable aerosol models,
361 which further results a persistent overestimation in DT algorithm (Che et al. 2019). By the additional
362 radiometric and polarimetric correction, the DPC GRASP/Model showed good performance over
363 both Land and Ocean. The high values of AOD in the South China Sea and the estuary of the Yangtze
364 River can be clearly captured. To summarized, the DPC showed spatial ability of AOD retrieval
365 based on GRASP algorithm in China region and the similar results have also been reported recently
366 by using the GRASP/component module (Li et al. 2022).

367 Another case was selected in Western Europe where the air is clean and aerosol loading is low
368 (< 0.2) in the most of time around year. As shown in **Figure 6b**, different satellites and aerosol
369 retrieval methods showed slightly different distributions of AOD. In addition to the different transit
370 times between DPC and MODIS, this phenomenon is also probably because the aerosol signal is
371 difficult to separate from the totally satellite observation under low aerosol loading conditions and
372 thus result relative larger uncertainties of retrieval. From the AOD maps of DPC GRASP/Model,
373 the relatively high values of AOD (~ 0.25) were found in Central France, Southern Spain, and
374 Southern England. While, the MODIS MAIAC showed lower AOD (~ 0.1) over the mainland and



375 two points of high AOD (~ 0.5) were found in Northern coastal areas of Spain and Algeria. By
376 contrast, the distributions of AOD calculated by DT and DB algorithm were also different from that
377 calculated by DPC GRASP/Model and MAIAC. The high AOD (~ 0.4) region appeared in Northern
378 France, Italy, and Southern England. Compared with single pixel-based retrieval algorithm (such as
379 DT and DB), the GRASP and MAIAC considered more temporal and spatial information of aerosol
380 and surface parameters. All of them have been proven to have good performance of AOD retrieval
381 (Sayer et al. 2014; Lyapustin et al. 2018; Chen et al. 2020; Ou et al. 2021).

382 4.3 Comparison of DPC AOD with MODIS Products at a Temporal Scale

383 In this section, time-series of AOD were evaluated by compared with MODIS aerosol products
384 based on the observations of AERONET site. The mean error ratios (MER) were calculated for the
385 global collocation data set from 23 selected AERONET stations, as shown in **Figure 7**. The MER
386 compares the mean bias for each satellite aerosol products in a specified period of time to their EE%
387 (Gupta et al. 2018). Lower absolute value of MER means the smaller actual errors, indicating a good
388 match with the AERONET. The selected AERONET stations had relatively continuous observations
389 during the study period to avoid that global validation statistics shift in local emphasis and introduce
390 temporal variation in the global results (Gupta et al. 2018). From the **Figure 7**, it was found that the
391 time series of AOD from DPC GRASP/Model had a good matching with the AERONET AOD. The
392 absolute values of MER were stable and less than ~ 0.05 after day 65. While the reason of relatively
393 large negative MER (~ -0.1) before day 65 is presumed to be low EE%, as the DPC GRASP/Model
394 would underestimate AOD under heavy aerosol loading conditions. This result is similar to the result
395 of DT algorithm. Both showed good performances. In addition, the temporal averaged MER showed
396 that the MODIS DT (0.0230) and DPC GRASP/Model (0.0049) generally overestimated the AOD,
397 while the MODIS MAIAC (-0.0208) underestimated. By contrast, though the temporal averaged
398 MER of MODIS DB was closer to 0, this was due to the cancellation between positive and negative
399 biases. It is worth noting that the same parameter scheme (including start points and constraints)
400 was applied globally in the GRASP/Model. Therefore, the difference in aerosol optical properties
401 and spatial-temporal heterogeneity in different regions may be not considered appropriately. The
402 optimization of the region is expected to improve the inversion effect.

403 **Figure 8** showed three cases at different underlying surface to display the time series of AOD
404 retrieved from DPC GRASP/Model on the basis of AERONET observations. The DT AOD was also
405 compared as a reference, due to its stable performance. It was found that the behavior of AOD from
406 DPC/GRASP and MODIS DT was generally consistent with AERONET at the three sites. From the
407 scatterplots, the values of R were 0.983 and 0.928, 0.943 and 0.959, and 0.967 and 0.859 for MODIS
408 DT and DPC GRASP/Model at Pilar_Cordob, Magurele_Inoe, and FZJ-JOYCE, respectively. The
409 GRASP/Model AOD retrieved from DPC were slightly higher than the AERONET in the FZJ-
410 JOYCE site and thus it resulted a relatively lower R. Nevertheless, in general, DPC/GRASP has a
411 good ability to capture the temporal variation of aerosols.

412 Conclusion and Summary

413 The DPC/ GaoFen-5 is the first multi-angular polarized sensor launched by China and thus it
414 has occupied an important position in the development of satellite sensors. In this study, AOD was
415 retrieved from the DPC images by using the GRASP algorithm and compared with AERONET and



416 MODIS observations. The main purpose is to evaluate the performance of the DPC to monitor global
417 aerosols.

418 On a global basis, a uniform parameterization scheme, which defined the variation ranges and
419 start values of the optical and microphysical properties (realized by aerosol type) of the aerosol, was
420 applied in the “Model” module of GRASP. Validations against AERONET showed that the R and
421 EE% of DPC GRASP/Model were 0.8590 and 79.68%, respectively, in the first attempt. The SCA,
422 number of averaged pixels in retrieval units, and fitting residual showed an impact on the results of
423 AOD. A larger number of pixels in retrieval units and a smaller fitting residual can help improve the
424 quality of retrieval. By quality control (SCA > 150, number of averaged pixels < 4, non-polarized
425 fitting residual < 8%, and 0.01 < polarized fitting residual < 0.08 removed), the R and EE% of DPC
426 GRASP/Model improve to 0.8982 and 83.16%, respectively. The corresponding MB and NMSE
427 decreased from 0.0189 and 0.1432 to 0.0176 and 0.1008, respectively. This indicated that DPC has
428 a good ability to detect aerosols under this scheme.

429 In the perspective of spatial scale, the R and EE% of GRASP/Model were larger than 0.9 and
430 80% respectively in the most AERONET sites. Large NMSE and Low EE were found in low aerosol
431 loading conditions such as west of the United States. When the actual AOD is small, the retrieval
432 bias of AOD from satellite observations will be amplified as reflected in NMSE and EE to some
433 extent. By compared with MODIS aerosol products, the AOD from DPC GRASP/Model showed
434 good consistency in China, that all regions with high AOD values were detected. Evaluation of the
435 time-serial AOD showed the performance of DPC GRASP/Model is similar to the MODIS DT and
436 better than MODIS DB and MAIAC products. Therefore, to summarize, the DPC can capture spatial
437 and temporal variations in aerosols. The study improves to our understanding of DPC and find a
438 solution for retrieving AOD based on GRASP algorithm. The continuous development of multi-
439 angle sensors polarized plays an important role in aerosol monitoring in the future.

440 **Acknowledgement**

441 This study was funded by the National Key R&D Program of China (Grant No. 2018YFB0504500),
442 National Natural Science Foundation of China (Grant No. 41875038, No. 42071348, and No.
443 42001291), the Key R&D projects in Hubei Province (Grant No. 2021BCA220) and supported by
444 the LIESMARS Special Research Funding. We are grateful to the Moderate Resolution Imaging
445 Spectroradiometer (MODIS) Team, the Aerosol Robotic Network (AERONET) Organization and
446 the GaoFen-5 Directional Polarimetric Camera (DPC) Developed Team for freely distributed their
447 aerosol products and measurements. The numerical calculations in this paper have been done on the
448 supercomputing system in the Supercomputing Center of Wuhan University. Finally, we would also
449 like to thank all reviewers for their constructive and valuable comments.

450 **References**

- 451 Albrecht, B.A. (1989). AEROSOLS, CLOUD MICROPHYSICS, AND FRACTIONAL CLOUDINESS.
452 *Science*, 245, 1227-1230
- 453 Ångström, A. (1964). The Parameter of Atmospheric Turbidity. *Tellus*, 14
- 454 Breon, F.M., & Colzy, S. (1999). Cloud detection from the spaceborne POLDER instrument and



- 455 validation against surface synoptic observations. *Journal of Applied Meteorology*, *38*, 777-785
- 456 Breon, F.M., & Goloub, P. (1998). Cloud droplet effective radius from spaceborne polarization
457 measurements. *Geophysical Research Letters*, *25*, 1879-1882
- 458 Che, H., Yang, L., Liu, C., Xia, X., Wang, Y., Wang, H., Wang, H., Lu, X., & Zhang, X. (2019). Long-
459 term validation of MODIS C6 and C6.1 Dark Target aerosol products over China using CARSNET and
460 AERONET. *Chemosphere*, *236*, 124268
- 461 Chen, C., Dubovik, O., Fuertes, D., Litvinov, P., Lapyonok, T., Lopatin, A., Ducos, F., Derimian, Y.,
462 Herman, M., Tanré, D., Remer, L.A., Lyapustin, A., Sayer, A.M., Levy, R.C., Hsu, N.C., Descloitres, J.,
463 Li, L., Torres, B., Karol, Y., Herrera, M., Herreras, M., Aspetsberger, M., Wanzenboeck, M., Bindreiter,
464 L., Marth, D., Hangler, A., & Federspiel, C. (2020). Validation of GRASP algorithm product from
465 POLDER/PARASOL data and assessment of multi-angular polarimetry potential for aerosol monitoring.
466 *Earth System Science Data*, *12*, 3573-3620
- 467 Cox, C., & Munk, W. (1954). Measurement Of The Roughness Of The Sea Surface From Photographs
468 Of The Sun's Glitter. *Journal Of The Optical Society Of America*, *44*, 838-850
- 469 D'Almeida, G.A., Koepke, P., & Shettle, E.P. (1991). Atmospheric aerosols: Global climatology and
470 radiative characteristics. *Journal of Medical Microbiology*, *54*, 55-61
- 471 Deschamps, P., Breon, F., Leroy, M., Podaire, A., Bricaud, A., Buriez, J., & Seze, G. (1994). The
472 POLDER mission: instrument characteristics and scientific objectives. *Ieee Transactions on Geoscience
473 and Remote Sensing*, *32*, 598-615
- 474 Deuzé, J.L., Bréon, F.M., Devaux, C., Goloub, P., Herman, M., Lafrance, B., Maignan, F., Marchand, A.,
475 Nadal, F., Perry, G., & Tanré, D. (2001). Remote sensing of aerosols over land surfaces from POLDER-
476 ADEOS-1 polarized measurements. *Journal of Geophysical Research: Atmospheres*, *106*, 4913-4926
- 477 Diner, D.J., Beckert, J.C., Reilly, T.H., Bruegge, C.J., Conel, J.E., Kahn, R.A., Martonchik, J.V.,
478 Ackerman, T.P., Davies, R., Gerstl, S.A.W., Gordon, H.R., Muller, J.P., Myneni, R.B., Sellers, P.J., Pinty,
479 B., & Verstraete, M.M. (1998). Multi-angle Imaging SpectroRadiometer (MISR) - Instrument description
480 and experiment overview. *Ieee Transactions on Geoscience and Remote Sensing*, *36*, 1072-1087
- 481 Dubovik, Sinyuk, A., Lapyonok, T., Holben, B.N., Mishchenko, M., Yang, P., Eck, T.F., Volten, H.,
482 Munoz, O., & Veihelmann, B. (2006). Application of light scattering by spheroids for accounting for
483 particle non-sphericity in remote sensing of desert dust. *Journal of Geophysical Research Atmospheres*,
484 *111*
- 485 Dubovik, O., Fuertes, D., Litvinov, P., Lopatin, A., Lapyonok, T., Dubovik, I., Xu, F., Ducos, F., Chen,
486 C., Torres, B., Derimian, Y., Li, L., Herreras-Giralda, M., Herrera, M., Karol, Y., Matar, C., Schuster,
487 G.L., Espinosa, R., Puthukkudy, A., Li, Z., Fischer, J., Preusker, R., Cuesta, J., Kreuter, A., Cede, A.,
488 Aspetsberger, M., Marth, D., Bindreiter, L., Hangler, A., Lanzinger, V., Holter, C., & Federspiel, C.
489 (2021). A Comprehensive Description of Multi-Term LSM for Applying Multiple a Priori Constraints in
490 Problems of Atmospheric Remote Sensing: GRASP Algorithm, Concept, and Applications. *Frontiers in
491 Remote Sensing*, *2*
- 492 Dubovik, O., Herman, M., Holdak, A., Lapyonok, T., Tanre, D., Deuze, J.L., Ducos, F., Sinyuk, A., &
493 Lopatin, A. (2011). Statistically optimized inversion algorithm for enhanced retrieval of aerosol
494 properties from spectral multi-angle polarimetric satellite observations. *Atmospheric Measurement
495 Techniques*, *4*, 975-1018
- 496 Dubovik, O., & King, M.D. (2000). A flexible inversion algorithm for retrieval of aerosol optical
497 properties from Sun and sky radiance measurements. *Journal of Geophysical Research Atmospheres*, *105*,
498 20673-20696



- 499 Dubovik, O., Lapyonok, T., Litvinov, P., Herman, M., Fuertes, D., Ducos, F., Lopatin, A., Chaikovskiy,
500 A., Torres, B., Derimian, Y., Huang, X., Aspetsberger, M., & Federspiel, C. (2014). GRASP: a versatile
501 algorithm for characterizing the atmosphere. *SPIE Newsroom*
- 502 Eck, T.F., Holben, B.N., Reid, J.S., Dubovik, O., Smirnov, A., O'Neill, N.T., Slutsker, I., & Kinne, S.
503 (1999). Wavelength dependence of the optical depth of biomass burning, urban, and desert dust aerosols.
504 *Journal of Geophysical Research: Atmospheres*, *104*, 31333-31349
- 505 Eck, T.F., Holben, B.N., Sinyuk, A., Pinker, R.T., Goloub, P., Chen, H., Chatenet, B., Li, Z., Singh, R.P.,
506 Tripathi, S.N., Reid, J.S., Giles, D.M., Dubovik, O., O'Neill, N.T., Smirnov, A., Wang, P., & Xia, X.
507 (2010). Climatological aspects of the optical properties of fine/coarse mode aerosol mixtures. *Journal of*
508 *Geophysical Research*, *115*
- 509 Gao, J., Woodward, A., Vardoulakis, S., Kovats, S., Wilkinson, P., Li, L., Xu, L., Li, J., Yang, J., Li, J.,
510 Cao, L., Liu, X., Wu, H., & Liu, Q. (2017). Haze, public health and mitigation measures in China: A
511 review of the current evidence for further policy response. *Science of the Total Environment*, *578*, 148-
512 157
- 513 Ge, B., Mei, X., Li, Z., Hou, W., Xie, Y., Zhang, Y., Xu, H., Li, K., & Wei, Y. (2020). An improved
514 algorithm for retrieving high resolution fine-mode aerosol based on polarized satellite data: Application
515 and validation for POLDER-3. *Remote Sensing of Environment*, *247*
- 516 Goloub, P., & Deuze, J.L. (1994). Analysis of the POLDER polarization measurements performed over
517 cloud covers. *IEEE Trans.geosci.remote Sens*, *32*, 78-88
- 518 Gomez-Chova, L., Camps-Valls, G., Calpe-Maravilla, J., Guanter, L., & Moreno, J. (2007). Cloud-
519 screening algorithm for ENVISAT/MERIS multispectral images. *Ieee Transactions on Geoscience and*
520 *Remote Sensing*, *45*, 4105-4118
- 521 Guo, J., Deng, M., Lee, S.S., Wang, F., Li, Z., Zhai, P., Liu, H., Lv, W., Yao, W., & Li, X. (2016). Delaying
522 precipitation and lightning by air pollution over the Pearl River Delta. Part I: Observational analyses.
523 *Journal of Geophysical Research: Atmospheres*, *121*, 6472-6488
- 524 Gupta, P., Remer, L.A., Levy, R.C., & Mattoo, S. (2018). Validation of MODIS 3 km land aerosol optical
525 depth from NASA's EOS Terra and Aqua missions. *Atmospheric Measurement Techniques*, *11*, 3145-
526 3159
- 527 Hagolle, O., Goloub, P., Deschamps, P.-Y., Cosnefroy, H., Briottet, X., Bailleul, T., Nicolas, J.-M., Parol,
528 F., Lafrance, B., & Herman, M. (1999). Results of POLDER in-flight calibration. *Ieee Transactions on*
529 *Geoscience and Remote Sensing*, *37*, 1550-1566
- 530 Holben, B.N., Eck, T.F., Slutsker, I., Tanre, D., Buis, J.P., Setzer, A., Vermote, E., Reagan, J.A., Kaufman,
531 Y.J., Nakajima, T., Lavenu, F., Jankowiak, I., & Smirnov, A. (1998). AERONET - A federated instrument
532 network and data archive for aerosol characterization. *Remote Sensing of Environment*, *66*, 1-16
- 533 Hsu, N.C., Jeong, M.J., Bettenhausen, C., Sayer, A.M., Hansell, R., Seftor, C.S., Huang, J., & Tsay, S.C.
534 (2013). Enhanced Deep Blue aerosol retrieval algorithm: The second generation. *Journal of Geophysical*
535 *Research: Atmospheres*, *118*, 9296-9315
- 536 Hsu, N.C., Tsay, S.C., King, M.D., & Herman, J.R. (2004). Aerosol properties over bright-reflecting
537 source regions. *IEEE Transactions on Geoscience & Remote Sensing*, *42*, 557-569
- 538 Jin, S., Ma, Y., Zhang, M., Gong, W., Dubovik, O., Liu, B., Shi, Y., & Yang, C. (2019). Retrieval of 500
539 m Aerosol Optical Depths from MODIS Measurements over Urban Surfaces under Heavy Aerosol
540 Loading Conditions in Winter. *Remote Sensing*, *11*, 2218
- 541 Jin, S., Zhang, M., Ma, Y., Gong, W., Chen, C., Yang, L., Hu, X., Liu, B., Chen, N., Du, B., & Shi, Y.
542 (2021). Adapting the Dark Target Algorithm to Advanced MERSI Sensor on the FengYun-3-D Satellite:



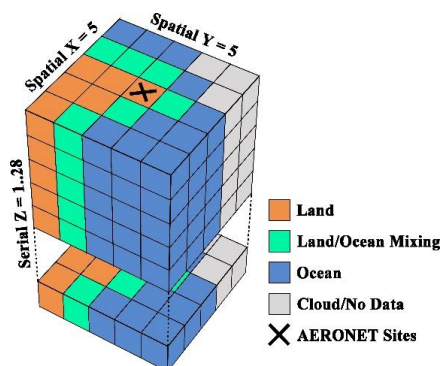
- 543 Retrieval and Validation of Aerosol Optical Depth Over Land. *Ieee Transactions on Geoscience and*
544 *Remote Sensing*, 59, 8781-8797
- 545 Kacenelenbogen, M., Leon, J.F., Chiapello, I., & Tanre, D. (2006). Characterization of aerosol pollution
546 events in France using ground-based and POLDER-2 satellite data. *Atmospheric Chemistry and Physics*,
547 6, 4843-4849
- 548 Kaufman, Y.J., Tanré, D., Gordon, H.R., Nakajima, T., Lenoble, J., Frouin, R., Grassl, H., Herman, B.M.,
549 King, M.D., & Teillet, P.M. (1997). Passive remote sensing of tropospheric aerosol and atmospheric
550 correction for the aerosol effect. *Journal of Geophysical Research: Atmospheres*, 102, 16815-16830
- 551 Koren, I., Remer, L.A., Kaufman, Y.J., Rudich, Y., & Martins, J.V. (2007). On the twilight zone between
552 clouds and aerosols. *Geophysical Research Letters*, 34, 5
- 553 Lenoble, J., Remer, L., & Tanre, D. (2013). *Aerosol Remote Sensing*. Springer-Verlag Berlin Heidelberg
- 554 Levy, R.C., Mattoo, S., Munchak, L.A., Remer, L.A., Sayer, A.M., Patadia, F., & Hsu, N.C. (2013). The
555 Collection 6 MODIS aerosol products over land and ocean. *Atmospheric Measurement Techniques*, 6,
556 2989-3034
- 557 Li, J.H., Ma, J.J., Li, C., Wang, Y.Y., Li, Z.Q., & Hong, J. (2021). Multi-information collaborative cloud
558 identification algorithm in Gaofen-5 Directional Polarimetric Camera imagery. *Journal of Quantitative*
559 *Spectroscopy & Radiative Transfer*, 261
- 560 Li, L., Che, H., Zhang, X., Chen, C., Chen, X., Gui, K., Liang, Y., Wang, F., Derimian, Y., Fuertes, D.,
561 Dubovik, O., Zheng, Y., Zhang, L., Guo, B., Wang, Y., & Zhang, X. (2022). A satellite-measured view of
562 aerosol component content and optical property in a haze-polluted case over North China Plain.
563 *Atmospheric Research*, 266, 105958
- 564 Li, L., Dubovik, O., Derimian, Y., Schuster, G.L., Lapyonok, T., Litvinov, P., Ducos, F., Fuertes, D., Chen,
565 C., Li, Z., Lopatin, A., Torres, B., & Che, H. (2019). Retrieval of aerosol components directly from
566 satellite and ground-based measurements. *Atmospheric Chemistry and Physics*, 19, 13409-13443
- 567 Li, X.W., Gao, F., Wang, J.D., & Strahler, A. (2001). A priori knowledge accumulation and its application
568 to linear BRDF model inversion. *Journal of Geophysical Research-Atmospheres*, 106, 11925-11935
- 569 Li, Z., Hou, W., Hong, J., Zheng, F., Luo, D., Wang, J., Gu, X., & Qiao, Y. (2018). Directional
570 Polarimetric Camera (DPC): Monitoring aerosol spectral optical properties over land from satellite
571 observation. *Journal of Quantitative Spectroscopy and Radiative Transfer*, 218, 21-37
- 572 Li, Z.Q., Lau, W.K.M., Ramanathan, V., Wu, G., Ding, Y., Manoj, M.G., Liu, J., Qian, Y., Li, J., Zhou,
573 T., Fan, J., Rosenfeld, D., Ming, Y., Wang, Y., Huang, J., Wang, B., Xu, X., Lee, S.S., Cribb, M., Zhang,
574 F., Yang, X., Zhao, C., Takemura, T., Wang, K., Xia, X., Yin, Y., Zhang, H., Guo, J., Zhai, P.M., Sugimoto,
575 N., Babu, S.S., & Brasseur, G.P. (2016). Aerosol and monsoon climate interactions over Asia. *Reviews*
576 *of Geophysics*, 54, 866-929
- 577 Lopatin, A., Dubovik, O., Fuertes, D., Stenchikov, G., Lapyonok, T., Veselovskii, I., Wienhold, F.G.,
578 Shevchenko, I., Hu, Q., & Parajuli, S. (2021). Synergy processing of diverse ground-based remote
579 sensing and in situ data using the GRASP algorithm: applications to radiometer, lidar and radiosonde
580 observations. *Atmos. Meas. Tech.*, 14, 2575-2614
- 581 Lyapustin, A., Wang, Y., Korkin, S., & Dong, H. (2018). MODIS Collection 6 MAIAC algorithm.
582 *Atmospheric Measurement Techniques*, 11, 5741-5765
- 583 Ma, Y., Zhu, Y., Liu, B., Li, H., Jin, S., Zhang, Y., Fan, R., & Gong, W. (2021). Estimation of the vertical
584 distribution of particle matter (PM_{2.5}) concentration and its transport flux from lidar measurements
585 based on machine learning algorithms. *Atmospheric Chemistry and Physics*, 21, 17003-17016
- 586 Martins, J.V., Tanré, D., Remer, L., Kaufman, Y., Mattoo, S., & Levy, R. (2002). MODIS Cloud screening



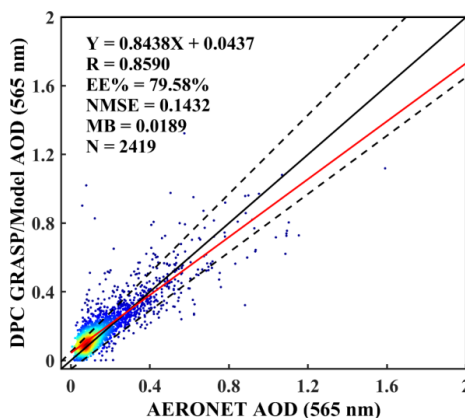
- 587 for remote sensing of aerosols over oceans using spatial variability. *Geophysical Research Letters*, 29
588 McCormick, M.P., Hamill, P., Pepin, T.J., Chu, W.P., Swissler, T.J., & McMaster, L.R. (1979).
589 SATELLITE STUDIES OF THE STRATOSPHERIC AEROSOL. *Bulletin of the American*
590 *Meteorological Society*, 60, 1038-1046
- 591 Mishchenko, M.I., & Travis, L.D. (1997). Satellite retrieval of aerosol properties over the ocean using
592 polarization as well as intensity of reflected sunlight. *Journal of Geophysical Research: Atmospheres*,
593 102, 16989-17013
- 594 Nadal, F., & Bréon, F.M. (1999). Parameterization of Surface Polarized Reflectance Derived from
595 POLDER Spaceborne Measurements. *IEEE Transactions on Geoscience & Remote Sensing*, 37, 1709-
596 1718
- 597 Nakajima, T., Yoon, S.C., Ramanathan, V., Shi, G.Y., Takemura, T., Higurashi, A., Takamura, T., Aoki,
598 K., Sohn, B.J., Kim, S.W., Tsuruta, H., Sugimoto, N., Shimizu, A., Tanimoto, H., Sawa, Y., Lin, N.H.,
599 Lee, C.T., Goto, D., & Schutgens, N. (2007). Overview of the Atmospheric Brown Cloud East Asian
600 Regional Experiment 2005 and a study of the aerosol direct radiative forcing in east Asia. *Journal of*
601 *Geophysical Research-Atmospheres*, 112, 23
- 602 Ou, Y., Li, L., Ying, Z., Dubovik, O., Derimian, Y., Chen, C., Fuertes, D., Xie, Y., Lopatin, A., Ducos, F.,
603 & Peng, Z. (2021). Spatio-Temporal Variability of Aerosol Components, Their Optical and
604 Microphysical Properties over North China during Winter Haze in 2012, as Derived from
605 POLDER/PARASOL Satellite Observations. *Remote Sensing*, 13, 2682
- 606 Qie, L., Li, Z., Zhu, S., Xu, H., Xie, Y., Qiao, R., Hong, J., & Tu, B. (2021). In-flight radiometric and
607 polarimetric calibration of the Directional Polarimetric Camera onboard the GaoFen-5 satellite over the
608 ocean. *Appl Opt*, 60, 7186-7199
- 609 Rao, C.R.N., Stowe, L.L., & McClain, E.P. (1989). REMOTE-SENSING OF AEROSOLS OVER THE
610 OCEANS USING AVHRR DATA THEORY, PRACTICE AND APPLICATIONS. *International Journal*
611 *of Remote Sensing*, 10, 743-749
- 612 Remer, L.A., Mattoo, S., Levy, R.C., Heidinger, A., Pierce, R.B., & Chin, M. (2012). Retrieving aerosol
613 in a cloudy environment: aerosol product availability as a function of spatial resolution. *Atmospheric*
614 *Measurement Techniques*, 5, 1823-1840
- 615 Rosenfeld, D., Lohmann, U., Raga, G.B., O'Dowd, C.D., Kulmala, M., Fuzzi, S., Reissell, A., & Andreae,
616 M.O. (2008). Flood or drought: How do aerosols affect precipitation? *Science*, 321, 1309-1313
- 617 Sayer, A.M., Hsu, N.C., Bettenhausen, C., & Jeong, M.J. (2013). Validation and uncertainty estimates
618 for MODIS Collection 6 "Deep Blue" aerosol data. *Journal of Geophysical Research: Atmospheres*, 118,
619 7864-7872
- 620 Sayer, A.M., Munchak, L.A., Hsu, N.C., Levy, R.C., Bettenhausen, C., & Jeong, M.J. (2014). MODIS
621 Collection 6 aerosol products: Comparison between Aqua's e-Deep Blue, Dark Target, and "merged" data
622 sets, and usage recommendations. *Journal of Geophysical Research-Atmospheres*, 119, 13965-13989
- 623 Shi, T., Han, G., Ma, X., Gong, W., Chen, W., Liu, J., Zhang, X., Pei, Z., Gou, H., & Bu, L. (2021).
624 Quantifying CO₂ Uptakes Over Oceans Using LIDAR: A Tentative Experiment in Bohai Bay.
625 *Geophysical Research Letters*, 48, e2020GL091160
- 626 Tanre, D., Breon, F.M., Deuze, J.L., Dubovik, O., Ducos, F., Francois, P., Goloub, P., Herman, M.,
627 Lifermann, A., & Waquet, F. (2011). Remote sensing of aerosols by using polarized, directional and
628 spectral measurements within the A-Train: the PARASOL mission. *Atmospheric Measurement*
629 *Techniques*, 4, 1383-1395
- 630 Tegen, I., & Lacis, A.A. (1996). Modeling of particle size distribution and its influence on the radiative



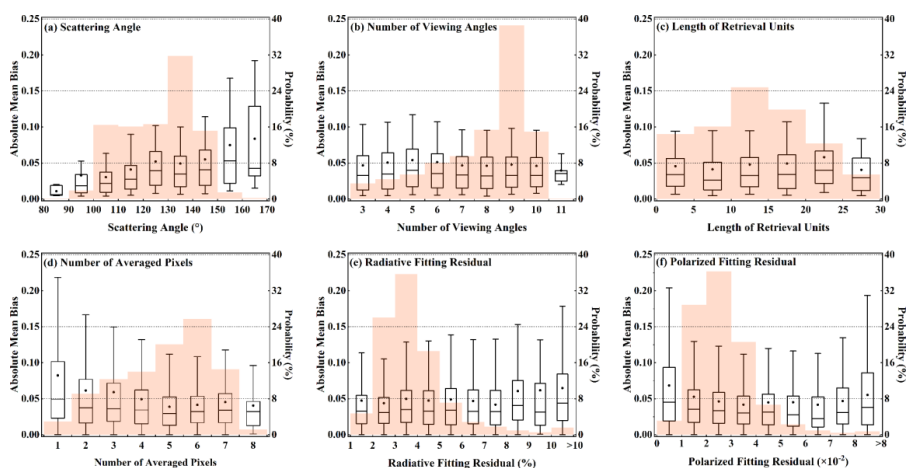
631 properties of mineral dust aerosol. *Journal of Geophysical Research Atmospheres*, *101*, 19237-19244
632 Zhang, M., Jin, S., Ma, Y., Fan, R., Wang, L., Gong, W., & Liu, B. (2021). Haze events at different levels
633 in winters: A comprehensive study of meteorological factors, Aerosol characteristics and direct radiative
634 forcing in megacities of north and central China. *Atmospheric Environment*, *245*, 118056
635 Zhdanova, E.Y., Chubarova, N.Y., & Lyapustin, A.I. (2020). Assessment of urban aerosol pollution over
636 the Moscow megacity by the MAIAC aerosol product. *Atmospheric Measurement Techniques*, *13*, 877-
637 891
638 Zhu, S., Li, Z., Qie, L., Xu, H., Ge, B., Xie, Y., Qiao, R., Xie, Y., Hong, J., Meng, B., Tu, B., & Chen, F.
639 (2022). In-Flight Relative Radiometric Calibration of a Wide Field of View Directional Polarimetric
640 Camera Based on the Rayleigh Scattering over Ocean. *Remote Sensing*, *14*
641



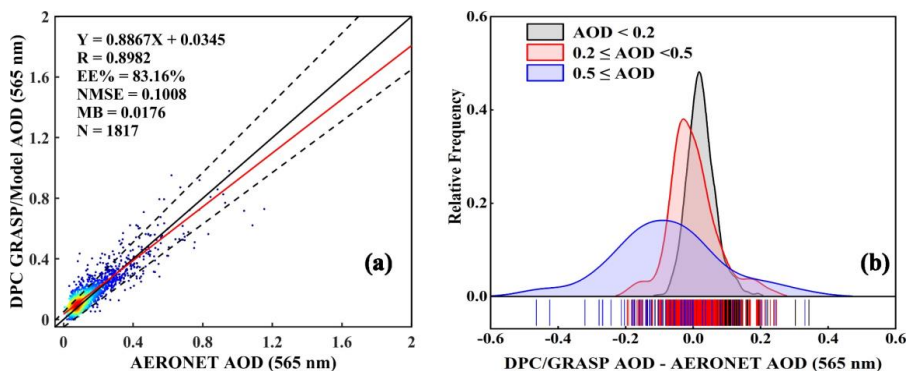
642
643 **Figure 1.** Schematic diagram for multi-pixel retrieval unit (5×5×1..28). A maximum of 28 sequences
644 allowed in each unit is limited by hardware memory.
645



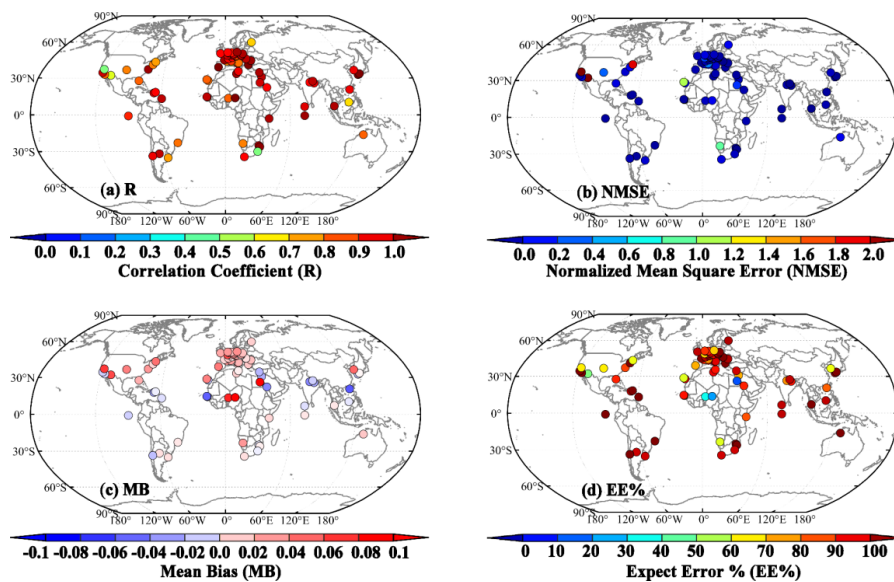
646
647 **Figure 2.** Two-dimensional density scatterplot of AOD retrieval from DPC with the GRASP/Model
648 scheme versus the AERONET observations. The solid black lines are diagonal and the dashed black
649 lines show the ranges of expect error. The red solid lines represent the linear regression lines.
650



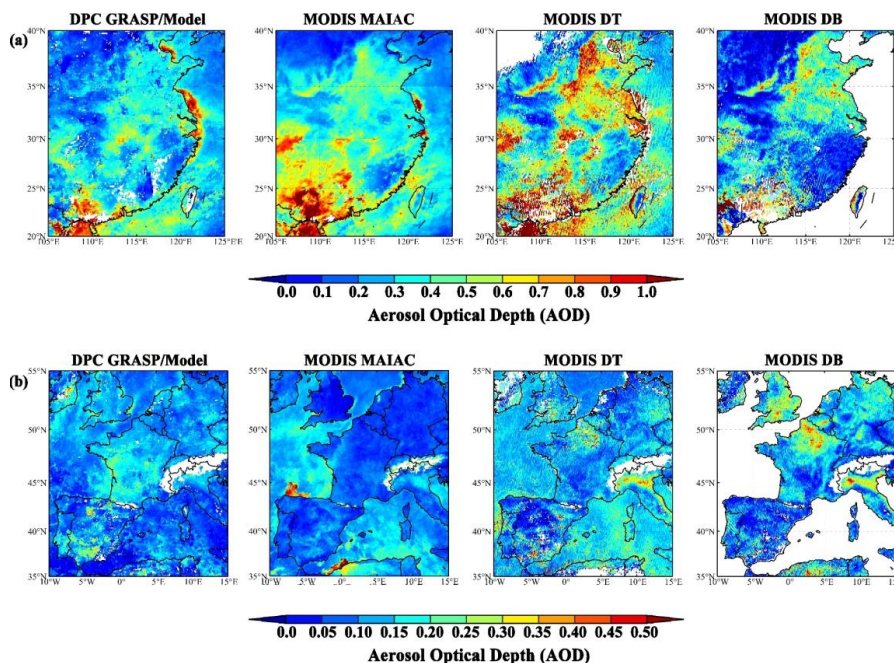
651
 652 **Figure 3.** Influencing factors of AOD retrieval performance of DPC based on the GRASP/Model:
 653 **(a)** SCA; **(b)** number of viewing angles; **(c)** length of retrieval units; **(d)** number of averaged pixels;
 654 **(e)** non-polarized fitting residual; **(f)** polarized fitting residual. Orange shadows in the background
 655 represents the probability distribution of the samples.
 656



657
 658 **Figure 4.** Performances of AOD retrieval from DPC data based on the GRASP/Model after quality
 659 control. **(a)** Two-dimensional density scatterplot of AOD retrieval from DPC with the GRASP
 660 algorithm versus the AERONET observations; **(b)** Relative Frequency of AOD differences between
 661 DPC/GRASP and AERONET.
 662



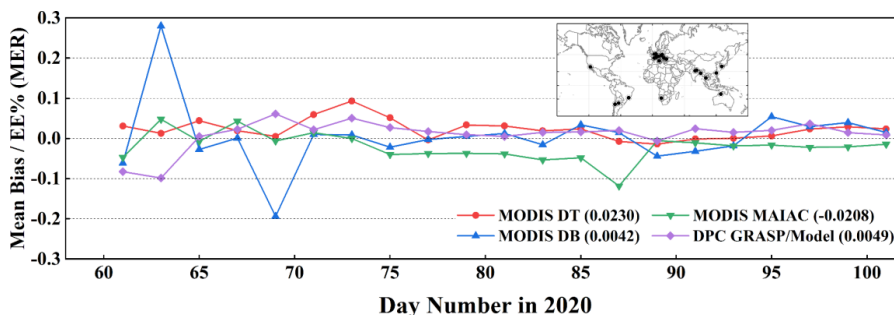
663
 664 **Figure 5.** Spatial Distributions of (a) R, (b) NMSE, (c) MB, and (d) EE% calculated from DPC
 665 GRASP/model by compared with AERONET observations. Only sites with more than 10 matching
 666 points are included.
 667



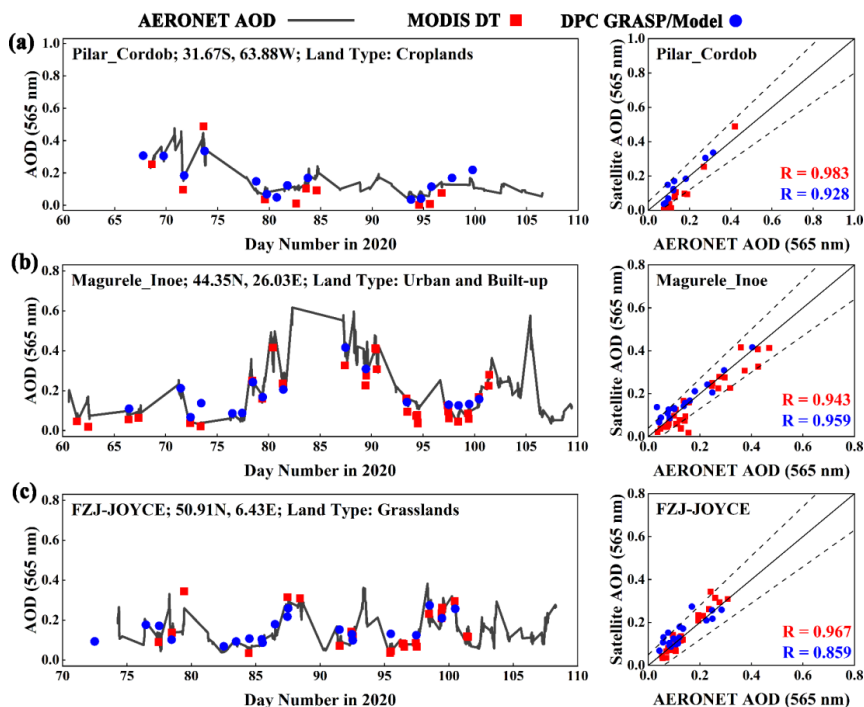
668
 669 **Figure 6.** Spatial distribution of AOD from DPC GRASP/Model compared with MODIS MAIAC,
 670 DT, and DB aerosol products in March, 2020: (a) Eastern and Southern China with its adjacent sea
 671 areas. The dashed line is part of the Nine-dotted Line; (b) Areas of Western Europe including the



672 Atlantic Ocean and the Mediterranean. The DPC AOD is at 565 nm and the MODIS AOD is at 550
 673 nm.
 674



675
 676 **Figure 7.** Time series of mean error ratios (MER) for the global collocation data set from 23 selected
 677 AERONET stations during March and April of 2020. The number in brackets are temporal averaged
 678 values of MER. The map inset shows the positions of AERONET stations with more details.
 679



680
 681 **Figure 8.** Time series of AOD from the DPC GRASP/Model versus the MODIS DT products and
 682 AERONET observations at three sites as cases: (a) Pilar_Cordob, (b) Magurele_Inoe, and (c) FZJ-
 683 JOYCE. The scatterplot shows the relationship between AERONET AOD and satellite AOD.
 684